Annals of Biomedical Engineering, Vol. 36, No. 11, November 2008 (© 2008) pp. 1856–1869
DOI: 10.1007/s10439-008-9557-1

Fluid Dynamics of Gas Exchange in High-Frequency Oscillatory Ventilation: *In Vitro* Investigations in Idealized and Anatomically Realistic Airway Bifurcation Models

KEVIN B. HERATY,[1,2] JOHN G. LAFFEY,[3,4] and NATHAN J. QUINLAN[1,2]

[1]Department of Mechanical and Biomedical Engineering, National University of Ireland Galway, Galway, Ireland; [2]National Centre for Biomedical Engineering Science, National University of Ireland Galway, Galway, Ireland; [3]Lung Biology Group, National Centre for Biomedical Engineering Science, National University of Ireland Galway, Galway, Ireland; and [4]Department of Anaesthesia, Galway University Hospitals, Galway, Ireland

(*Received 1 November 2007; accepted 25 August 2008; published online 11 September 2008*)

Abstract—The objective of this work is to develop understanding of the local fluid dynamic mechanisms that underpin gas exchange in high-frequency oscillatory ventilation (HFOV). The flow field during HFOV was investigated experimentally using particle image velocimetry in idealized and realistic models of a single bifurcation. Results show that inspiratory and expiratory fluid streams coexist in the airway at flow reversal, and mixing between them is enhanced by secondary flow and by vortices associated with shear layers. Unsteady flow separation and recirculation occurs in both geometries. The magnitude of secondary flow is greater in the realistic model than in the idealized model, and the structure of secondary flow is quite different. However, other flow structures are qualitatively similar.

Keywords—Respiratory flow, Mechanical ventilation, Lung, Particle image velocimetry.

INTRODUCTION

The aim of this study is to develop an improved understanding of the fluid dynamics of high-frequency oscillatory ventilation (HFOV). HFOV is a shallow, fast mode of mechanical ventilation which can avoid the risk of lung injury associated with cyclic opening and closing of alveolar units in conventional ventilation.[16] HFOV has been successfully applied to neonates since 1981,[18] and more recently to adolescents[20] and adults.[1,6,19] HFOV results in better pulmonary outcomes than conventional mechanical ventilation for very low birth weight infants suffering with respiratory distress syndrome.[27] In adults suffering from acute respiratory distress syndrome (ARDS), Derdak *et al.*[6] showed that HFOV is at least as effective as conventional ventilation strategy. However, HFOV remains a relatively new and incompletely understood mode of ventilation. An improved fundamental understanding of gas exchange in HFOV is essential in order to harness its potential to improve outcome in patients with ARDS.

Breathing frequencies from 60 to 2400 breaths per minute with tidal volumes of 35–150 mL have been used in HFOV,[16] whereas in normal breathing, the typical rate is 12 breaths per minute with a tidal volume of 500 mL. The anatomical dead space (the volume of the conducting airways) is approximately 150 mL. In normal breathing, therefore, 350 mL of the inspired 500 mL is transported to the alveoli for gas exchange. In HFOV, however, since the tidal volume is usually less than the anatomical dead space, gas exchange cannot be explained in terms of simple advective bulk transport to the alveoli.

More detailed knowledge of HFOV fluid dynamics is essential in order to develop HFOV systems and strategies that optimize gas exchange, and potentially improve outcome from acute lung injury (ALI) and ARDS. It is apparent from previous research that Taylor dispersion and secondary flow, particularly at flow reversal, have a significant impact on dispersion, and hence on the effectiveness of gas exchange in HFOV. Collectively, these can be classified as convective phenomena which act locally (within an individual bifurcation) to enhance axial mixing (that is, mixing between O_2-rich gas in upper regions of the airway and CO_2-rich gas in lower regions). The purpose of this study is to develop a better understanding of these fluid dynamic mechanisms and their interactions in HFOV.

This paper describes an investigation of the fluid dynamics of HFOV at the level of a single airway

Address correspondence to Nathan J. Quinlan, Department of Mechanical and Biomedical Engineering, National University of Ireland Galway, Galway, Ireland. Electronic mail: nathan.quinlan@nuigalway.ie

bifurcation. The goal is to identify and understand localized fluid dynamic mechanisms which augment bulk transport by promoting mixing in the axial direction. Two-component particle image velocimetry (PIV) and stereoscopic particle image velocimetry (SPIV) were used to measure the flow field quantitatively in *in vitro* models of a single bifurcation at flow conditions representative of HFOV in the upper airway. Models were scaled up to enhance the effective spatial and temporal resolution of the measurements. To identify and differentiate flow phenomena with the greatest possible clarity, experiments were carried out first in an idealized geometry. Measurements were also made in a realistic geometry, in order to investigate the effects of nonideal geometry on flow structures.

METHODS

The idealized and realistic geometry models are shown in Fig. 1. The idealized model consists of a single symmetric bifurcation with the geometry defined by Comer *et al.*,[5] based on the morphological work of Weibel.[34] The flow divider is rounded with a radius of 0.1 times the diameter of the daughter branch. The realistic model is based on images of a third-generation airway bifurcation from the inferior lobar bronchus of the left lung. The images were acquired from the female data set of the Visible Human Project®.[2] Images were manipulated with image processing and surface modeling software (Mimics® and Rhinoceros®, respectively) to generate a three-dimensional geometric description of a third-generation lung bifurcation. The parent and daughter branches have noncircular cross sections, and their centerlines are not coplanar and have slight three-dimensional curvature. The right and left daughter branches divide at 24° and 20° to the parent branch centerline, respectively. Extension sections have been added to all inflow and outflow ports of the realistic geometry. In the extension sections, there is a smooth transition from the realistic anatomical cross section of the airway branch to a circular cross section, allowing circular-section tubes to be coupled to the physical model for experimental testing. Using the surface modeling software, continuity was enforced across surface boundaries to avoid any steps, sharp edges, or curvature discontinuities.

To improve the spatial and temporal resolution of the experiment, the geometry was scaled up by a factor of 5.6. Thus, the parent branch diameter scaled from 5.3 mm in the third-generation lung airway to 30 mm in the experimental model. To ensure validity of the scaling by complete dynamic similarity, the Reynolds number Re (dimensionless velocity) and Womersley number α (dimensionless frequency) must be preserved in the scale models. This was enforced with a 59/41% (by volume) glycerol/water mixture as the working fluid along with reductions in flow velocity and oscillation frequency. The frequency reduction enhances the effective temporal resolution of the experiment by a factor of 56.2. The composition of the glycerol–water mixture is also influenced by optical considerations, as discussed below.

Tests were carried out for two Reynolds numbers, $Re = 740$ and 1480, and two Womersley numbers, $\alpha = 4.3$ and 7.0. The Womersley number $\alpha = D/2\,(2\pi f/\nu)^{1/2}$ characterizes the unsteadiness of oscillatory flows, where $D = 2a$ is the airway diameter, f is the frequency of oscillation of the flow, and ν is the kinematic viscosity. For $\alpha \ll 1$ the flow is quasi-steady, but for high α unsteady effects are important. In terms of clinical parameters, frequency is proportional to α^2 in a given geometry. Throughout this article, the Reynolds number $Re = UD/\nu$ is based on the mean velocity in

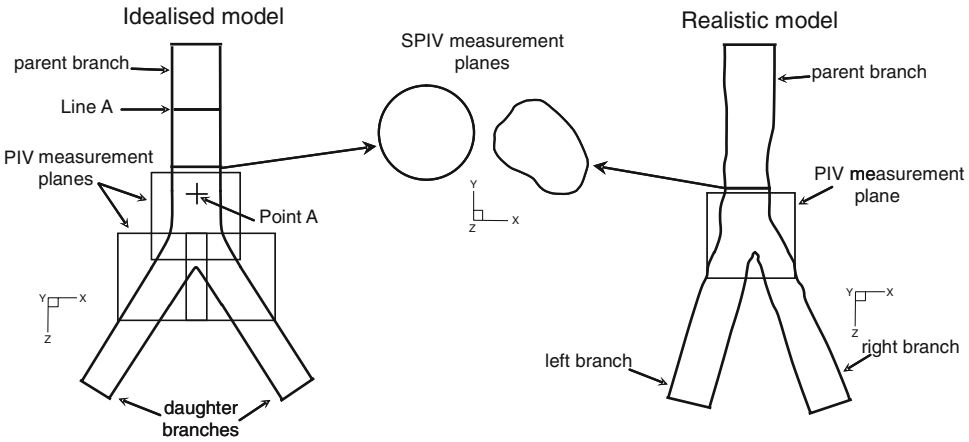

FIGURE 1. Geometrically accurate sectional views of the idealized and realistic experimental models, showing PIV and SPIV measurement locations.

the parent branch at peak inspiration, denoted by U. At the level of the third-generation airway, $Re = 1480$ and $\alpha = 4.3$ corresponds to a tidal volume of 47 mL through the trachea at 377 breaths/min, representative of a HFOV condition. The test cases may also be characterized in terms of a dimensionless flow amplitude, L/a, where L is the mean displacement of a fluid particle over one cycle, based on bulk transport, and a is the tube radius. The three dimensionless parameters are not independent, as $Re = \alpha^2 L/a$. The four test cases in this study are summarized in Table 1. All four test conditions fall within the flow regime dominated by the effects of convective acceleration, as defined by Jan *et al.*[14]

Rigid experimental models were made in Sylgard™ 184 (Dow Corning®) transparent silicone by a lost core technique described by Kelly *et al.*[15] The geometry of the experimental models was validated by comparing computed topography (CT) scans of the silicone models to the original CAD geometry models. Measurements were made at 118 cross sections in the idealized and realistic models, respectively, and it was found that the average cross-sectional area in the experimental models was 3% greater than in the original CAD geometry models.

TABLE 1. Summary of test conditions.

Test case	*Re*	α	*L/a*
1	740	4.3	40
2	740	7	15
3	1480	4.3	80
4	1480	7	30

The flow apparatus, shown in Fig. 2, supplied a controllable time-varying flow rate through the experimental model, while allowing unobstructed optical access for both two-component PIV and SPIV. A sinusoidal flow rate was applied to the experimental models by a custom-built computer-controlled piston pump, with a maximum stroke length of 1 m and a maximum stroke volume of 15.4 L. The pump was driven by a position-controlled stepper motor (Sanyo Denki Co. Ltd., 103-H8223-6540), which was controlled by a computer with a custom-designed LabVIEW™ 7 program.

Straight tubes were attached at all inflow and outflow ports of the experimental models to minimize entrance and exit effects. Gerrard and Hughes[10] found experimentally that oscillatory flow is fully developed

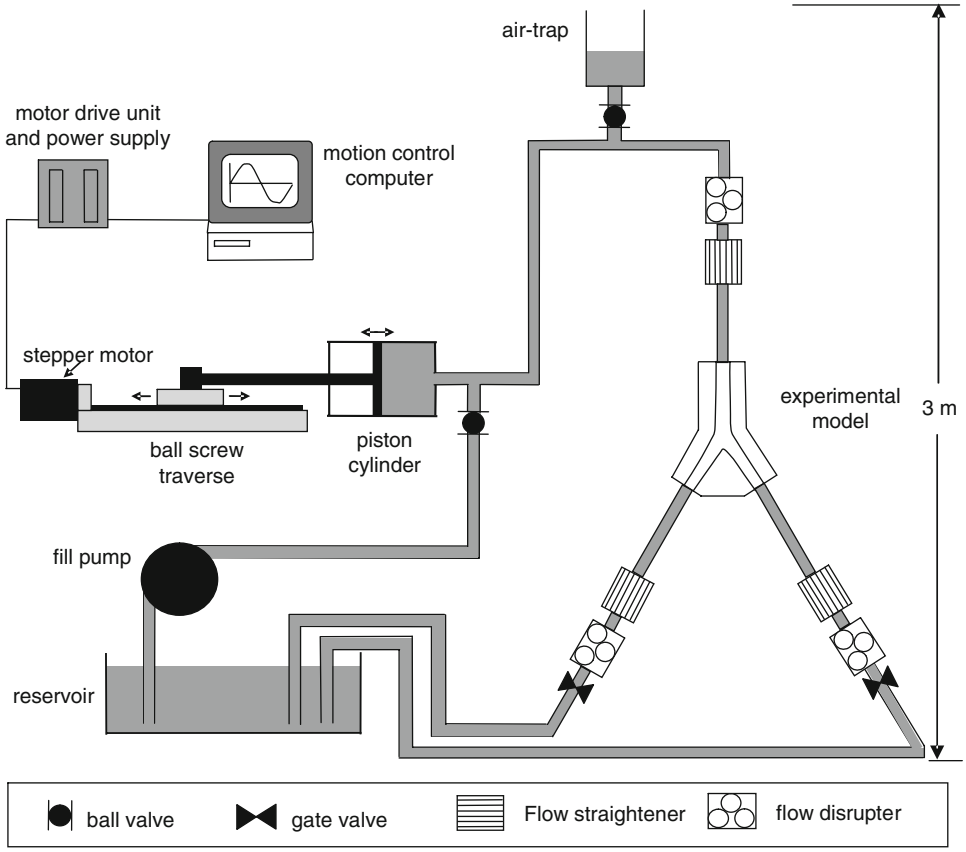

FIGURE 2. Schematic diagram of the experimental flow apparatus.

at a distance of $(0.08)a^2u_0/v$ from the tube entrance, where a is the tube radius, u_0 is the mean velocity based on peak flow, and v is the kinematic viscosity. The entrance tubes used in this study were 30% longer than the required entrance length.

A flow disrupter and a flow straightener were attached to each straight tube section as shown in Fig. 2, at the opposite end from the bifurcation model, to condition the intake flow from the pump or reservoir. Each flow disrupter consists of a short tube full of glass spheres. Their function is to provide a uniform axial velocity profile. Each flow straightener consists of a bundle of parallel small-bore thin-walled tubes, intended to remove any radial and swirl velocity components. Flow rates through the daughter branches of the idealized geometry were measured in steady expiratory flow using PIV, and were matched to within 1% by adjusting the gate valves shown in Fig. 2.

The refractive index of the working fluid and the Sylgard 184 silicone was measured at 20 °C using an Abbe refractometer with sodium D light, and was found to be 1.411 for both materials. Chrome-coated hollow glass tracer particles of diameter 10 μm were added to the fluid mixture.

Instantaneous full field measurements were made using two-component PIV and three-component SPIV at different locations. The plane of measurement was illuminated with Nd:YAG lasers (New Wave Research^{TM}, Gemini PIV Laser). Images were captured using a 1000 × 1016 pixel CCD camera (TSI, PIVCAM^{TM} 10–30) with 8-bit digitization.

Measurement was triggered at the start of inspiration for each cycle by an electronic switch mounted on the frame of the piston pump. All PIV images were processed using 32 × 32 pixel interrogation windows, and each interrogation window overlapped neighboring interrogation windows by 50%. A 32 × 32 pixel interrogation window corresponds to a 1.7 × 1.7 mm^2 region of the measurement plane. SPIV images were processed using 16 × 16 pixel interrogation windows with 50% overlap. Each 16 × 16 pixel interrogation window measured 1.5 × 1.5 mm^2. The velocity field was sampled at a rate of 7.5 Hz for tests at $\alpha = 4.3$ and at 15 Hz for $\alpha = 7.0$. According to the Nyquist theorem, this would allow measurement of fluctuations up to 3.25 and 7.5 Hz, respectively, or up to 29 and 26 times the base cycle frequency. Particle images were processed by two-frame cross-correlation using Insight 3G^{TM} 8.0.5 software.[13] Using the data of Raffel *et al.*,[25] measurement uncertainty for this PIV configuration was estimated as 0.007 m/s, or 1.6% of the peak flow velocity.

The two-component PIV measurements were calibrated using dimensions measured in CT images of the experimental models. The SPIV measurements were calibrated by placing a three-dimensional calibration target in the fluid-filled model at the measurement location. A correction procedure was implemented for all SPIV measurements using Insight 3G^{TM} 8.0.5 software[13] to reduce error due to misalignment between the calibration target and the measurement plane.

The locations of the measurement regions for the idealized and realistic geometries are illustrated in Fig. 1. In both experimental models, all two-component PIV measurements were acquired on a plane passing through the centers of the three inlet/outlet ports. This is defined as the xz plane in the Cartesian coordinate system shown in Fig. 1. This coordinate system is used throughout this article to indicate the relative orientation of measurement planes. For the idealized geometry, the z-axis corresponds exactly with the centerline of the parent branch. The outlines of the idealized and realistic models, shown in Fig. 1, are the intersections of these xz measurement planes with the silicone experimental models. Seven overlapping measurement regions, measuring 58 mm × 58 mm, were used in each geometry model to map the velocity field on the xz plane with two-component PIV. However, only those field measurements near the flow divider will be shown here. SPIV measurements were acquired on a number of xy planes (i.e., transverse sections) through the parent branch of each model, and results will be presented here for the measurement plane nearest the flow divider. PIV and SPIV measurements were captured at similar times, allowing PIV and SPIV results to be considered in association. All results are nondimensionalized with respect to U, the mean velocity in the parent branch at peak inspiration.

The velocity fields presented are phase-averaged over 6–10 cycles. The cycle-to-cycle variation in the mean velocity on line A at peak flow was 2% of the average (line A is a line parallel to the x axis, passing through the centerline of the parent branch, as shown in Fig. 1).

RESULTS

Detailed velocity measurements are presented in Figs. 3–6 for $L/a = 15$, $Re = 740$, and $\alpha = 7.0$. Qualitatively similar flow structures were observed for all test cases, and these results may be considered representative. Figures 3 and 4 illustrate the phase-averaged flow field in the idealized and realistic bifurcation geometries, at dimensionless times $\tau = 0.057$, 0.115, 0.452, and 0.623. τ is dimensionless time t/T, where $t = 0$ is at the start of inspiration, and T is the period. In the two-component PIV visualizations (Fig. 3), vectors represent the magnitude and direction of

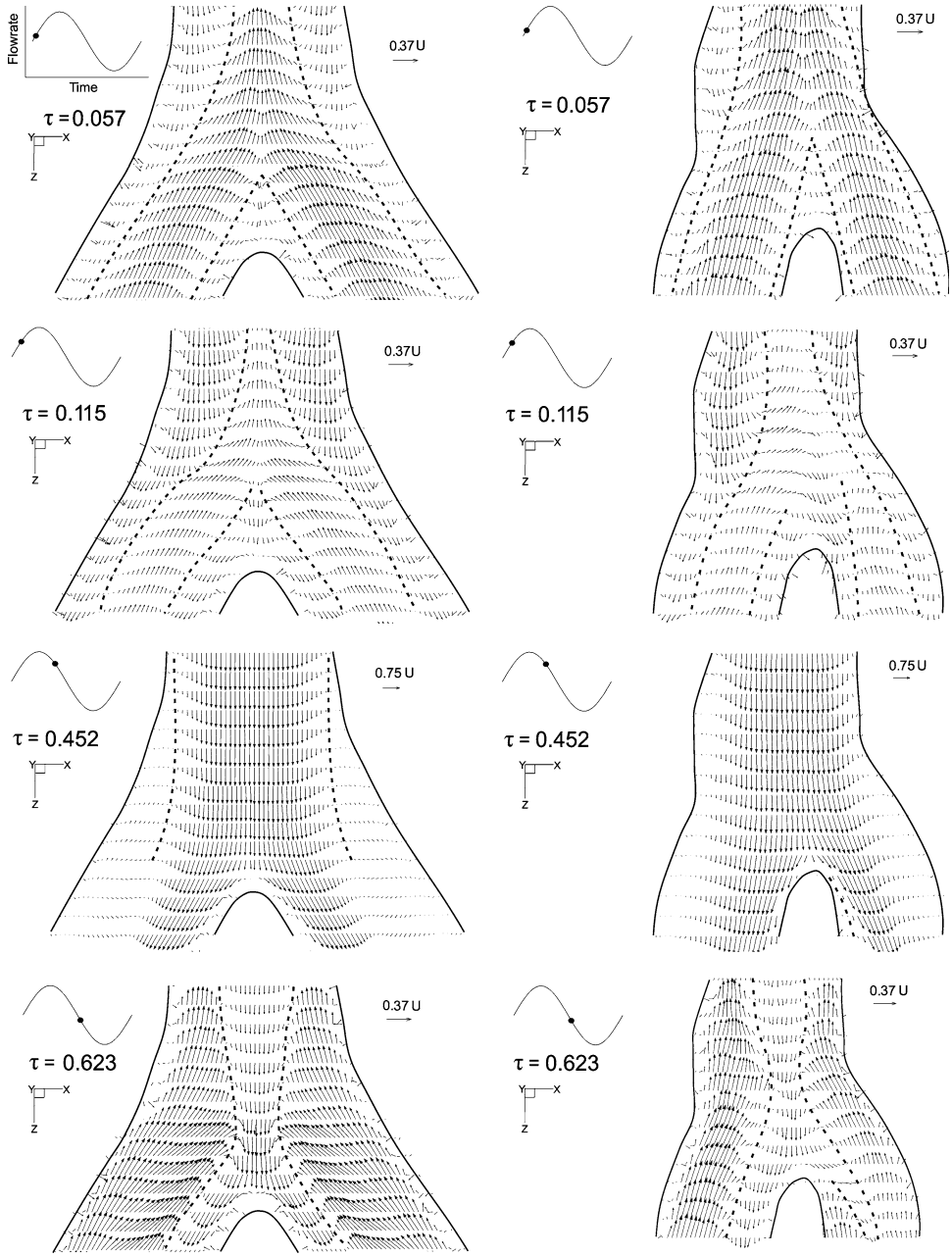

FIGURE 3. Nondimensionalized two-component PIV measurements in the idealized and realistic bifurcation models at *Lla* = 15, *Re* = 740, and α = 7.0. Dotted lines represent contours of zero velocity.

velocity. In the SPIV measurements (Fig. 4), the color map indicates the axial component (z-direction) of velocity (i.e., the component parallel to the nominal centerline of the parent branch) and the vectors indicate the magnitude and direction of the in-plane secondary flow.

Figure 3 illustrates the two-component velocity field measurements in the idealized and realistic bifurcation models. In both models at the beginning of inspiration ($\tau = 0.057$), the fluid at the walls reverses and begins to flow in the inspiration direction, while the faster-moving flow in the core of the airway continues to flow in the expiration direction, as in classical Womersley flow.[35] As a region of inspiratory flow develops near the walls, the shear layer between the opposing flows moves outwards from the wall. Figure 4 illustrates the three-component SPIV measurements. The shear layers are also evident in the stereoscopic measurement on the parent branch cross section. Throughout Figs. 3 and 4, the location of the shear layer is indicated approximately by the contour of zero z velocity. A secondary flow consisting of four longitudinal vortices

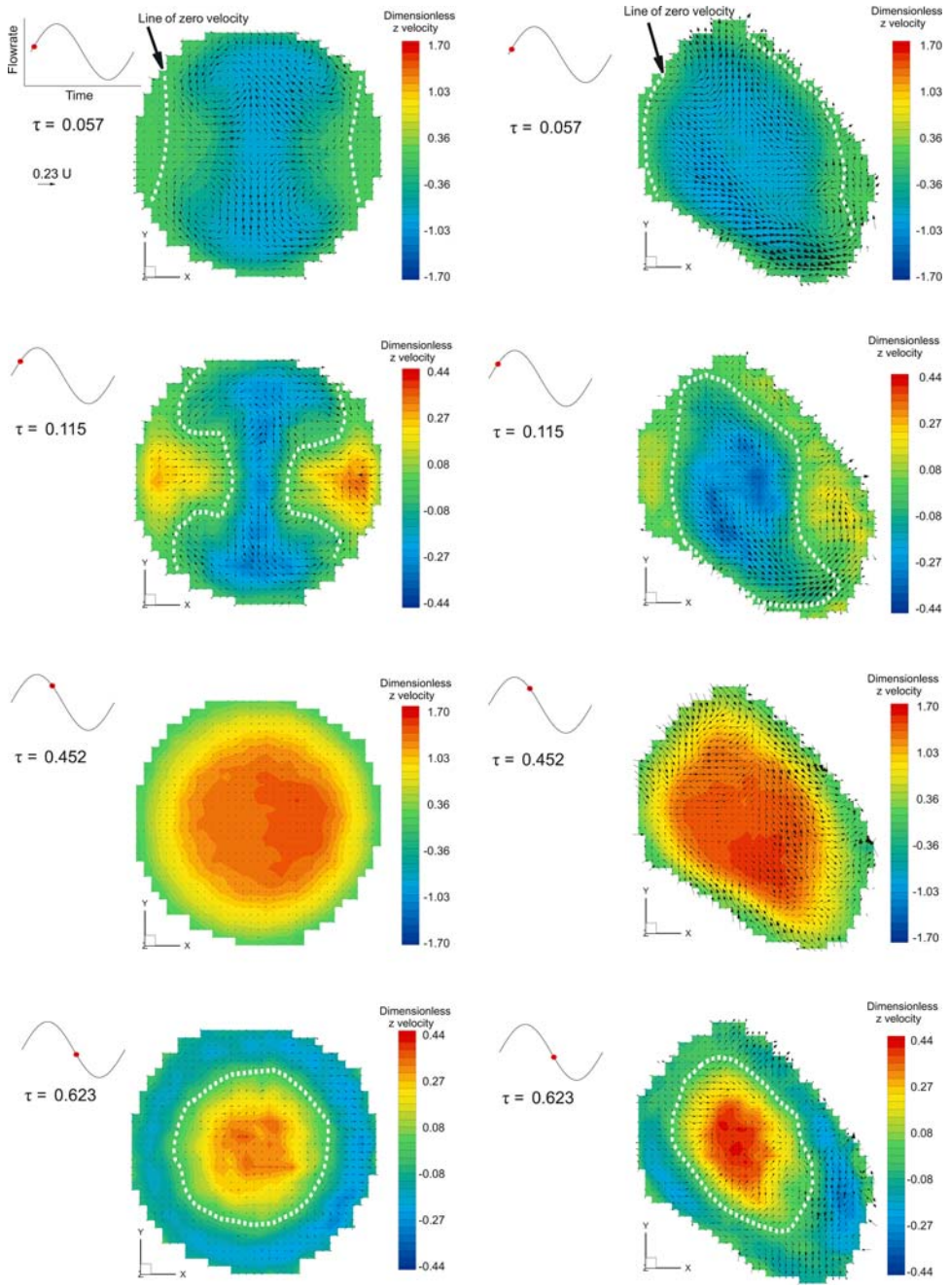

FIGURE 4. Nondimensionalized SPIV measurements in the idealized and realistic bifurcation models at *Ll*a = 15, *Re* = 740, and α = 7.0. Dotted lines are contours of zero axial velocity.

is present in the parent branch of the idealized model during expiration, as illustrated in the stereoscopic measurement (Fig. 4). These vortices are associated with the curvature of the daughter branches as they merge into the parent branch. Similar Dean-type vortical structures have been observed by other authors[8,14] during the expiration phase in idealized bifurcation models. In the stereoscopic view of the realistic model (Fig. 4) a single axial vortex is observed at the low y side of the cross section, and is superimposed on the inspiratory and expiratory fluid streams.

At $\tau = 0.115$ in the idealized geometry PIV measurement, the shear layers are observed closer to the core of the parent and daughter branches. The secondary flow vortical structures, observed at $\tau = 0.057$, are still present in the parent branch, but the vortices have moved closer to the core of the branch. It is apparent from the stereoscopic measurement that these

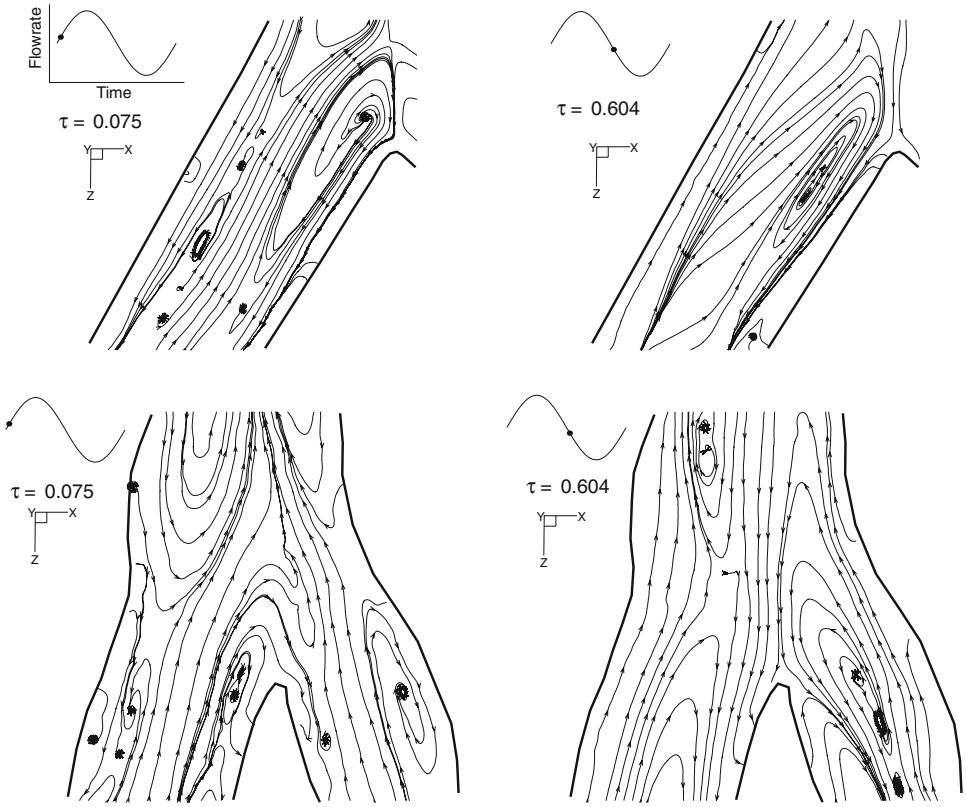

FIGURE 5. Instantaneous streamlines at both flow reversals in the idealized and realistic models.

vortices span the counterflowing inspiratory and expiratory streams. The stereoscopic measurement (Fig. 4) also indicates that the axial flow in the cross section is not axisymmetric at this location in the parent branch. At $\tau = 0.115$, inspiratory axial flow is observed first at the high and low x walls, but in the majority of the cross section, flow is in the negative z (expiratory) direction.

In the realistic model at $\tau = 0.115$, the shear layers are still present in the parent and daughter branches, but their structure has changed from that observed at $\tau = 0.057$. There is now a single shear layer in both the parent and left daughter branches, while a separate shear layer is observed in the right daughter branch. The corresponding stereoscopic measurement indicates that the shear layer in the parent branch is closer to the core of the branch than was observed at $\tau = 0.057$. An axial vortex structure is still present.

At peak inspiration in the idealized model at $\tau = 0.250$, all flow is in the direction of inspiration, and the structure is essentially quasi-steady. (The quasi-steady flow structure has been described in previous studies[17] and is not illustrated here.) At $\tau = 0.452$, when the flow is decelerating from peak inspiration, flow separates upstream of the bifurcation, and recirculation regions are created. However, the majority of the flow in the daughter branch is still in the inspiration direction. At $\tau = 0.623$, shortly after the mean flow reverses from inspiration to expiration, the slower-moving fluid at the walls of the parent branch and at the outer walls of the daughter branches is the first to change to the expiration direction. The faster-moving fluid in the core of the parent branch and at the inside walls of the daughter branches is still moving in the inspiration direction. Shear layers exist between these opposing fluid streams. The stereoscopic measurement in the parent branch (Fig. 4) confirms that the two shear layers visible in the two-component PIV measurement (Fig. 3) are part of a single cylindrical shear layer structure. The structure of the shear layers in both models near flow reversal is visualized in Fig. 5 using instantaneous streamlines, which were computed using Tecplot^{TM} 10 and initiated at points distributed throughout the bifurcation. In both geometry models, vortical structures are observed within the shear layers around both flow reversal times.

In the realistic model as the cycle reaches peak inspiration at $\tau = 0.25$, the flow structure resembles quasi-steady flow. A small recirculation region forms on the inside wall of the bifurcation in the right branch. This recirculation region is caused by the local curvature at the flow divider, as shown in Fig. 3 at $\tau = 0.452$. As the flow changes direction at the start of the expiration phase at $\tau = 0.623$, the slower moving

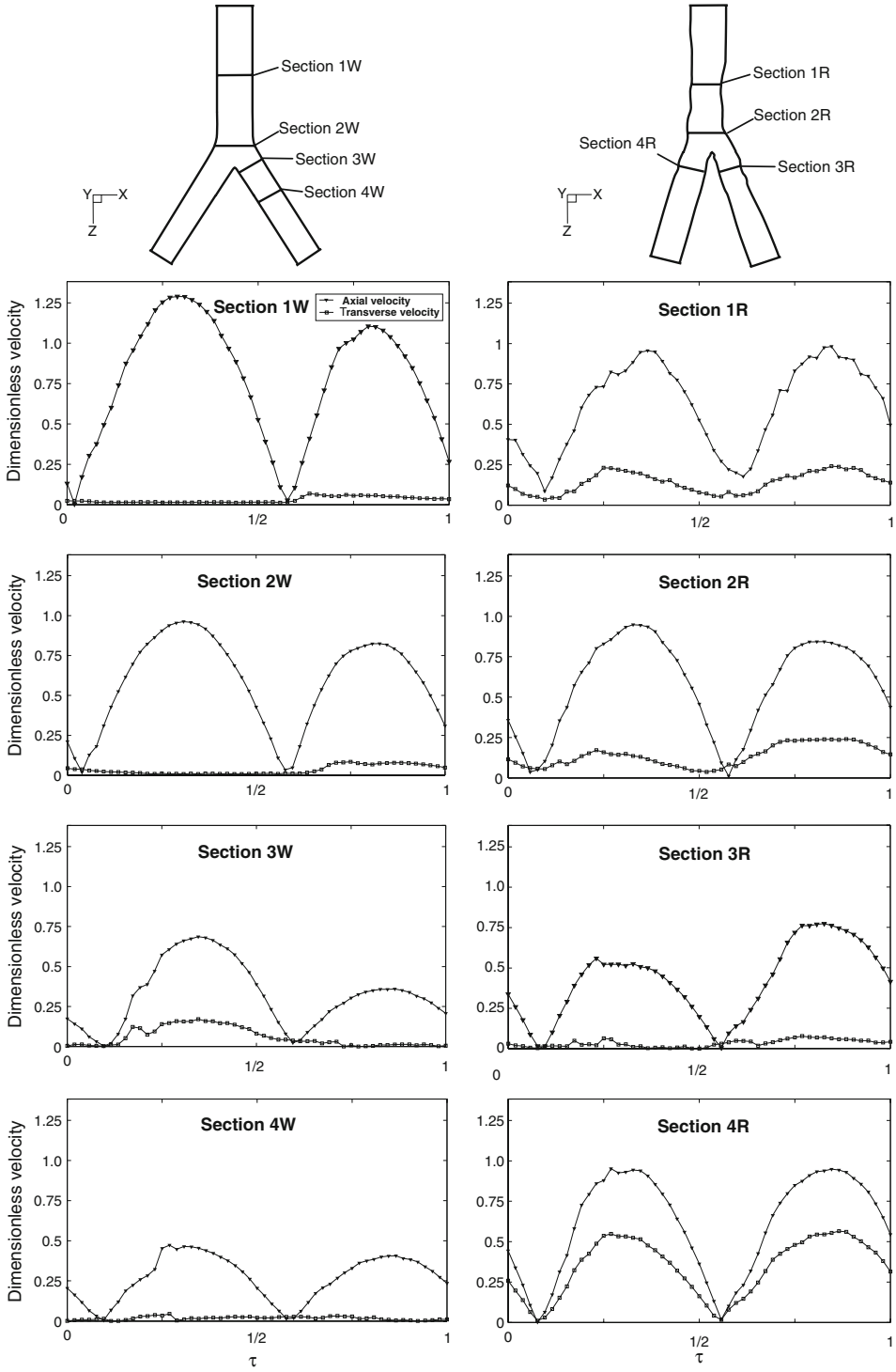

FIGURE 6. Magnitude of nondimensionalized axial and transverse velocity averaged over various transverse lines (indicated at the top of the figure) in the measurement plane in the parent and daughter branches of (a) idealized and (b) realistic models.

flow along the outer walls changes direction first, whereas the flow along the core of the parent and daughter branches is still moving in the inspiration direction. In the parent branch the shear layer is visible between the last of the inspiratory flow at the core of the branch and the expiratory flow at the perimeter.

The temporal variation of the mean magnitude of axial and transverse velocity at various section lines in the *xz* measurement plane is shown for both models in Fig. 6. The magnitude of transverse velocity is an indication of the level of secondary flow. At section 1W (in the parent branch of the idealized geometry),

axial velocity dominates for most of the HFOV cycle, except at times of flow reversal. The magnitude of transverse flow increases just after peak expiration, but remains small compared to the axial velocity. Closer to the bifurcation, at section 2W, the transverse velocity is 2% of the axial velocity at inspiration, and increases to 10% during the expiration phase. In the left daughter branch, at section 3W and 4W, the peak transverse velocity occurs during the inspiration phase. Transverse velocity is higher than axial velocity during flow reversal at the start of the expiration phase.

In the parent branch of the realistic geometry, at section 1R, the transverse velocity is 25% of axial velocity at peak inspiration and expiration. Closer to the bifurcation, at section 2R, the transverse velocity is 30% of the axial velocity at peak flow. Transverse velocity is greater than axial velocity in the parent branch at section 2R during periods of flow reversal. The transverse velocity measured in the right and left daughter branches is significantly different. In the left daughter branch at section 4R transverse velocity reached 59% of the axial velocity at peak flow, whereas only minimal levels are recorded in the right daughter branch at section 3R.

Qualitatively similar flow structures are observed at all four conditions tested ($15 \leq L/a \leq 80$, $Re = 740$, 1480, and $\alpha = 4.3$, 7.0). Shear layers are observed at all conditions. The duration of this counterflow increases as the flow becomes more strongly unsteady, from 14% of the cycle period at $\alpha = 4.3$ to 22% at $\alpha = 7.0$. At peak flow times, the velocity profile in the parent branch is flatter for $\alpha = 7.0$. Similar levels of transverse velocity are measured at all stations in both bifurcation models for $\alpha = 4.3$ and 7.0. For the two Reynolds numbers tested, the shear layers are present in the bifurcation for the same duration, but thinner shear layers with higher velocity gradients are observed at the higher Reynolds number.

Figure 7a shows the fluctuation of axial velocity over multiple cycles at Point A (Fig. 1) on the centerline of the parent branch in the idealized bifurcation model. At peak expiration (negative velocity), a high-frequency fluctuation can be observed. The amplitude of this velocity fluctuation is higher closer to flow divider. Figure 7b shows the phase-averaged velocity over ten cycles.

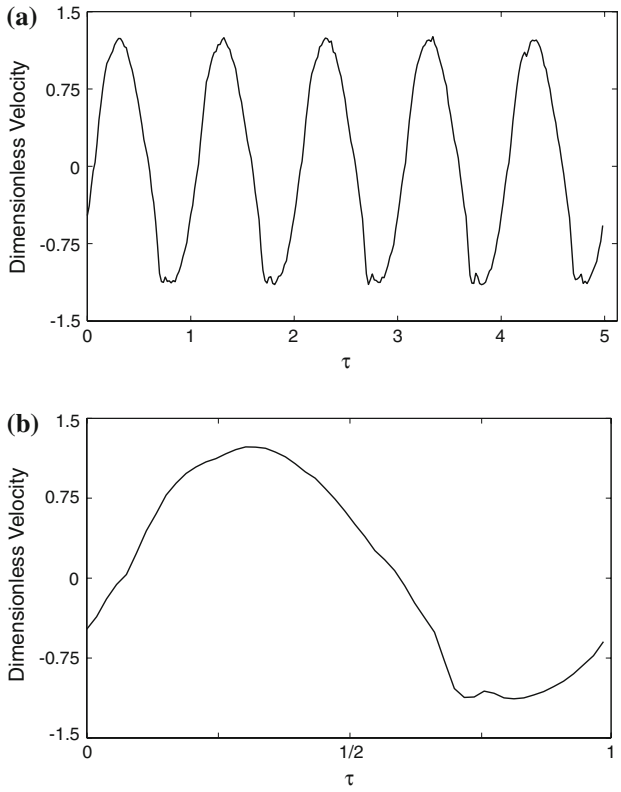

FIGURE 7. Axial velocity measured at Point A (Fig. 1) on the centerline of the parent branch of the idealized model, (a) over multiple cycles and (b) phase-averaged over ten cycles.

DISCUSSION

The aim of this study is to enhance understanding of local convective flow mechanisms in a respiratory bifurcation during HFOV. Several previous authors have reported pointwise velocity measurements in *in vitro* airway models using laser Doppler velocimetry (LDV).[17,24] Particle image velocimetry (PIV), as a whole-field technique, can potentially give clearer insight into the spatial structure of the flow. Ramuzat and Riethmuller[26] adopted PIV to study steady and oscillatory flows in airway models, and reported steady streaming effects. Many previous studies of fluid dynamics in HFOV have been based on idealized models of the airways, neglecting realistic geometric features such as curvature, asymmetric branching, and noncircular cross sections. However, the computational work of Nowak *et al.*[22] identified significantly different flow patterns in idealized and anatomically realistic airways under normal breathing conditions. Große *et al.*[11] highlighted the influence of geometric asymmetry of the realistic lung on normal respiratory airflow.

In the present work, two-component and stereoscopic (three-component) PIV were used in both idealized and realistic bifurcation models. An idealized geometry model was used to facilitate clear identification of the generic fluid dynamic phenomena in the mixing of inspired and expired air. An anatomically realistic model was used to explore the additional effects of realistic geometric features such as local curvature, nonuniform noncircular cross sections, and asymmetric branching angles.

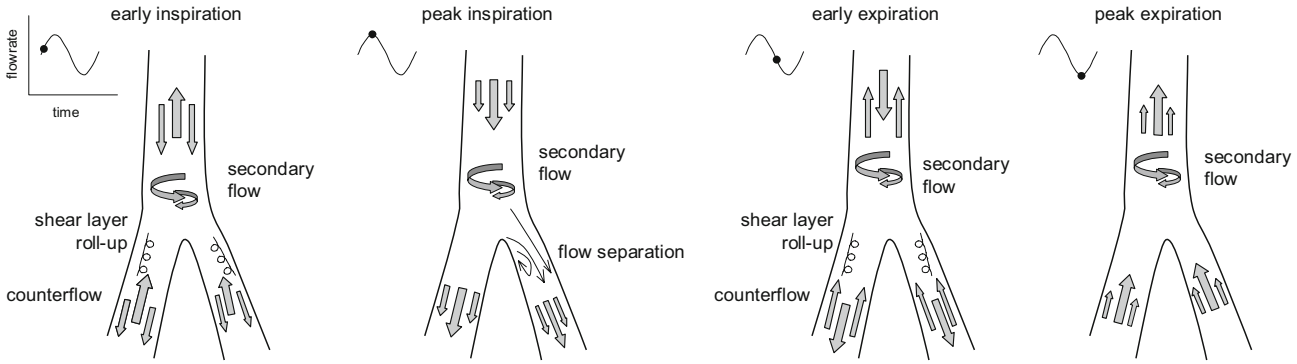

FIGURE 8. Sketch of the major flow structures observed in airway bifurcations throughout the cycle.

The most important observed flow phenomena are sketched in Fig. 8 for four key points in the cycle. The main features of the flow are common to both the idealized and realistic models and to all four flow conditions modeled. Quasi-steady flow exists only at times of peak flow, as other authors have also observed.[17]

Counterflow at Flow Reversal

One of the significant findings of this study is that inspiratory and expiratory fluid streams coexist in the airways for significant periods around flow reversal, as a result of the unsteadiness of the HFOV cycle. At $\alpha = 7.0$, counterflow and shear layers are present in both models for longer than in the less strongly unsteady case, $\alpha = 4.3$. At flow reversals in both models, shear layers appear between the inspiratory and expiratory streams. In the realistic model, these shear layers persist for slightly longer in the wider left daughter branch than in the right daughter branch. Vortical structures are apparent as a result of roll-up of shear layers in both models, illustrated by instantaneous streamlines shown in Fig. 5 and in the schematic diagram of Fig. 8.

Secondary Flow

The axial curvature of the idealized bifurcation results in a velocity profile skewed toward the inside wall of the flow divider and the generation of secondary flow structures in the daughter branches during inspiration. Lieber and Zhao[17] and Peattie and Schwarz[24] observed similar flow structures in idealized bifurcation geometries. Eckmann and Grotberg[7] observed a skewed velocity profile in a curved tube. Secondary flow longitudinal vortical structures are observed throughout the expiration phase and at flow reversal. Jan *et al.*[14] visualized a similar flow structure during the decelerating phase of expiration for $\alpha = 21.3$ and $L/a = 20$. More recently Fresconi *et al.*[8] observed a similar secondary flow pattern in the parent branch during expiration in a similar idealized bifurcation model. Significant levels of secondary flow are observed in the daughter branches during inspiration and in the parent branch during expiration, as shown in Fig. 6 at sections 1W and 2W.

In the realistic geometry, significant levels of secondary flow are observed during both inspiration and expiration in both parent and daughter branches. In the realistic model the parent and daughter branches have slight three-dimensional axial curvature, the daughter branches divide asymmetrically, and the walls are nonparallel. The curvature and nonparallel walls of the parent branch result in similar levels of secondary flow in the parent branch during inspiration and expiration, as seen in Fig. 6 at section 1R and section 2R. In inspiration, the skewed velocity profile and local wall curvature at the entrance of the right daughter branch cause a recirculation region. While the axial flow structure in the realistic bifurcation is similar to that observed in the idealized bifurcation, the nonplanar walls and slight three-dimensional axial curvature have a significant effect on the levels and structure of secondary flow.

Although axial and secondary flow structures in the idealized and realistic models are very different, the interaction between axial and secondary flow at flow reversals is similar in both models. In the parent branch of the realistic model, a single longitudinal vortex is observed, along with other more complex structure. This contrasts with the system of four vortices observed in the idealized geometry. In both models, the secondary flow vortices span the counterflowing inspiratory and expiratory flows at flow reversal.

Flow Separation

Flow separation with recirculation is observed in both the idealized and realistic bifurcation models at different times in the HFOV cycle. Recirculation in the realistic geometry results from separation due to the local curvature of the inside wall of the right daughter

branch during peak inspiration. In the idealized model, recirculation occurs on the outside of the bifurcation as the flow decelerates from peak inspiration, as shown in Fig. 3 for $\tau = 0.452$. Schroter and Sudlow[29] studied steady flow in an idealized bifurcation for $100 \leq Re \leq 4500$, and observed that the presence of recirculation regions was a function of the tube radius a of the parent branch and the radius of curvature R_c of the parent and daughter branch centerlines. They observed a region of recirculation in a model with $R_c \cong a$, but for $R_c = 4a$, no recirculation was observed. In the idealized geometry employed here, $R_c = (5.4)a$, and recirculation does not occur in the quasi-steady peak inspiration flow. Recirculation did not occur at any time in low-frequency oscillation experiments ($L/a = 634$, $Re = 740$, $\alpha = 1.08$; results not shown) in either geometry model. These observations are consistent with the findings of Schroter and Sudlow[29] for steady flow. Thus, the transient flow separation and recirculation observed in the present work appears to be an unsteady effect, dependent on Womersley number.

Instability

There is evidence of instability in the flow, in the form of high-frequency velocity fluctuations which were detected in the parent branch at peak expiration in the idealized geometry, as shown in Fig. 7a. These fluctuations vary from cycle to cycle, and do not appear in the phase-averaged velocity shown in Fig. 7b. This is consistent with the findings of Peattie and Schwarz,[24] who observed turbulent bursts in the parent branch of an idealized bifurcation at peak expiration.

Similar velocity fluctuations were observed in the realistic model on the parent branch centerline, at both peak inspiration and peak expiration. The magnitude of the fluctuations was highest near the flow divider in expiration, when a recirculation region forms between the fluid streams from the daughter branches. The temporal resolution of the PIV measurements in this study allows fluctuations at up to 26–29 times the cycle frequency to be resolved. As Peattie and Schwarz[24] detected fluctuations at 10–100 times the ventilation frequency, it is possible that some high-frequency fluctuations were beyond the resolution of the present experiments.

Significance for Mass Transport

The experimental results presented here describe the HFOV velocity field and flow structures in detail. However, concentration fields and mass transport effects have not been measured directly, and it is not possible to draw firm conclusions about respiratory mass transfer. Here we discuss the possible impact of some of the observed flow features on mass transport and gas exchange in HFOV, in light of previous research on mass transfer.

It is known that lateral mixing by secondary flows can play an important role in mass transport. Eckmann and Grotberg,[7] Fujioka *et al.*,[9] Nishida *et al.*,[21] and Tanaka *et al.*[30,31] have shown that effective diffusion is greater in curved and/or bifurcated tubes than in straight tubes for a range of conditions representative of HFOV, as a result of secondary flow. Tanaka *et al.*[31] also showed that significant transverse mixing occurred in an idealized model airway bifurcation at flow reversal, and found that a pause in the flow waveform around reversal allowed more time for transverse mixing, increasing the effective diffusivity by a factor of two. From these studies it is clear that the level of secondary flow has a significant effect on mass transport. Therefore, the enhanced levels of secondary flow due to axial curvature, asymmetric branching, and local wall curvature, measured in the realistic model in this study, could have important implications for mass transport in the lung. The interaction of secondary flow with axially counterflowing streams may be a further mechanism to enhance axial mass transport. However, this hypothesis requires further investigation to test and quantify.

In the upper airways, Taylor-type dispersion is a dominant mechanism.[4,16] Taylor (or shear-augmented) dispersion occurs when a nonuniform velocity profile in the airway causes differential rates of axial convection for fluid at different transverse locations.[32,33] At peak flow, a flattened velocity profile is observed in the parent branch of the idealized and realistic bifurcation models, as shown in Fig. 3. However, in off-peak flow, the velocity profile in the parent branch is less uniform and hence more conducive to Taylor dispersion.

The transient flow separation observed in these experiments may act as a convective mechanism to enhance axial mixing in oscillatory flow. Fluid particles which get trapped in a recirculation region are detained in the airway while the main stream passes by, and released for mixing later, when the flow separation breaks down. Thus, recirculating particles are effectively transferred upstream relative to the bulk motion of the main axial fluid stream. Direct measurement or computation of the concentration field will be required in future work to test and quantify the overall effect of this phenomenon on mass transport, as for the other flow phenomena discussed above.

Clinical Application

Acute lung injury and acute respiratory distress syndrome (ALI/ARDS) are severe inflammatory

diseases of the lung, and have a high morbidity and mortality. In fact, the mortality attributable to ALI in the United States is comparable to that seen with HIV infection, breast cancer, and asthma.[28] There is no cure for ALI/ARDS and the treatment is supportive. A key component of this supportive therapy is the mechanical support of respiration. Conventional mechanical ventilation strategies cause high lung stretch, and can damage lungs and contribute to mortality.[1] This has been a focus of intensive research effort in recent years, and has resulted in the development of 'low-stretch' ventilatory strategies, which have been demonstrated to save lives.[1]

HFOV has been widely used in the clinical setting for the management of the critically ill neonate and child. HFOV is increasingly used in adults with severe acutely injured lungs, where it performs comparably to leading edge 'protective' ventilation strategies.[1,6] However, our understanding of HFOV has advanced relatively little since its introduction into clinical practice in the late 1970s.[3] A better understanding of the mechanisms by which gas exchange occurs in HFOV offers the potential of developing more effective HFOV support therapies, by enhancing gas exchange while minimizing the potential for lung damage. Such novel HFOV strategies could significantly reduce death and disability from these devastating disease processes.

The research presented in this article offers new insights into the fluid dynamics of HFOV, which are a prerequisite for deep understanding of mass transport and gas exchange. In particular, the effect of complex realistic geometry on flow features has been investigated. In future work, these experimental results will be used to guide and validate high-resolution computational models, incorporating O_2 and CO_2 diffusion. Models of this type may be used to explore the design space for HFOV much more efficiently and safely than in preclinical and clinical trials, leading to opportunities for optimization of HFOV tidal volume, frequency, and waveform parameters.

Limitations

This study is based on *in vitro* models which have some inherent limitations. The models are rigid, and do not simulate dynamic deformations of the airway during the breathing cycle. However, this is a reasonable approximation for the upper conducting airway, in which deformation is restricted by the presence of cartilage in the walls.[23] A potentially more significant limitation of the present work is that models consist of a single tracheobronchial bifurcation. Previous studies of HFOV in the upper airway have shown that the flow structure in each bifurcation generation is influenced by the flow from higher and lower generations.[30] However, in a single-generation model, clearer insights into local fluid dynamics are possible without the added complexity of multigeneration effects. This fundamental approach was taken in the present work because a detailed understanding of flow in a single generation is a prerequisite for understanding of HFOV mechanisms in the lung as a whole.

CONCLUSION

In summary, we have shown that around times of flow reversal, inspiratory and expiratory flows co-exist throughout the bifurcation for substantial periods of the oscillatory cycle, and the duration of this counterflow increases as the oscillation frequency increases. Shear layers form between these counterflowing streams, leading to the formation of vortices, which could enhance mixing between the streams. Secondary flows, due to airway curvature and the flow between parent and daughter branches, also mix the inspiratory and expiratory streams. Unsteady flow separation and recirculation occur in both geometric models, at or just after peak flow, although it appears to be highly geometry dependent. Secondary flow velocity is significant in comparison with axial velocity at many times throughout the cycle, and greater than it in some cases near reversal. Secondary flow velocities are higher in the realistic geometry than in the idealized geometry, because of wall curvature. In the idealized geometry, the secondary flow in the parent branch resembles classical Dean vortices, but it is more complex in the realistic geometry. Axial velocity profiles are relatively flat at peak flow and most nonuniform at times of off-peak flow.

Understanding of the fluid dynamic mechanisms which underlie HFOV may ultimately contribute to the development of HFOV strategies to achieve more effective gas exchange, and ultimately increase survival in sufferers from ALI/ARDS. This work highlights the importance of transient counterflow, secondary flow, and recirculation, and also shows that realistic geometry features have a significant effect.

ACKNOWLEDGMENTS

The authors are grateful to Ms. Sue Harty and Dr. Gerard O'Sullivan of the Merlin Park Imaging Centre for providing CT images of the models. We also thank Mr. Colm Walsh and Mr. Kumar Saidha for their contributions to the development of the flow

apparatus. This research was supported by the Irish Research Council for Science, Engineering and Technology, funded by the National Development Plan; the Programme for Research in Third Level Institutions; and National University of Ireland, Galway through the Millennium Research Fund.

REFERENCES

[1]The Acute Respiratory Distress Syndrome Network. Ventilation with lower tidal volumes as compared with traditional tidal volumes for acute lung injury and the acute respiratory distress syndrome. *N. Engl. J. Med.* 342:1301–1308, 2000. doi:10.1056/NEJM200005043421801.

[2]Banvard, R. A. The Visible Human Project image data set from inception to completion and beyond. Proceedings of CODATA 2002: Frontiers of Scientific and Technical Data, Montreal, Canada, 2002.

[3]Bryan, A. C. The oscillations of HFO. *Am. J. Respir. Crit. Care Med.* 163:816–817, 2001.

[4]Chang, H. K. Mechanisms of gas transport during ventilation by high-frequency oscillation. *J. Appl. Physiol.* 56:553–563, 1984.

[5]Comer, J. K., C. Kleinstreuer, and Z. Zhang. Flow structures and particle deposition patterns in double-bifurcation airway models. Part 1. Air flow fields. *J. Fluid Mech.* 435:25–54, 2001. doi:10.1017/S0022112001003809.

[6]Derdak, S., S. Mehta, T. E. Stewart, T. Smith, M. Rogers, T. G. Buchman, B. Carlin, S. Lowson, J. Granton, and the Multicenter Oscillatory Ventilation for Acute Respiratory Distress Syndrome Trial (MOAT) Study Investigators. High-frequency oscillatory ventilation for acute respiratory distress syndrome in adults: a randomized, controlled trial. *Am. J. Respir. Crit. Care Med.* 166:801–808, 2002. doi:10.1164/rccm.2108052.

[7]Eckmann, D. M., and J. B. Grotberg. Oscillatory flow and mass transport in a curved tube. *J. Fluid Mech.* 188:509–527, 1988. doi:10.1017/S0022112088000825.

[8]Fresconi, F. E., A. S. Wexler, and A. K. Prasad. Expiration flow in a symmetric bifurcation. *Exp. Fluids* 35:493–501, 2003. doi:10.1007/s00348-003-0713-y.

[9]Fujioka, H., K. Oka, and K. Tanishita. Oscillatory flow and gas transport through a symmetrical bifurcation. *J. Biomech. Eng.* 123:145–153, 2001. doi:10.1115/1.1352735.

[10]Gerrard, J. H., and M. D. Hughes. The flow due to an oscillatory piston in a cylindrical tube: a comparison between experiment and a simple entrance flow theory. *J. Fluid Mech.* 50:97–106, 1971. doi:10.1017/S0022112071002477.

[11]Große, S., W. Schröder, M. Klaas, A. Klöckner, and J. Roggenkamp. Time resolved analysis of steady and oscillating flow in the upper human airways. *Exp. Fluids* 42:955–970, 2007. doi:10.1007/s00348-007-0318-y.

[12]Haselton, F. R., and P. W. Scherer. Flow visualization of steady streaming in oscillatory flow through a bifurcating tube. *J. Fluid Mech.* 123:315–333, 1982. doi:10.1017/S0022112082003085.

[13]Insight 3G^{TM} Data Acquisition Analysis and Display Software User Guide. Shoreview: TSI Inc., 2006.

[14]Jan, D. L., A. H. Shapiro, and R. D. Kamm. Some features of oscillatory flow in a model bifurcation. *J. Appl. Physiol.* 67:147–159, 1989.

[15]Kelly, J. T., A. K. Prasad, and A. S. Wexler. Detailed flow patterns in the nasal cavity. *J. Appl. Physiol.* 89:323–337, 2000.

[16]Krishnan, J. A., and R. G. Brower. High frequency ventilation for acute lung injury and ARDS. *Chest* 118:795–807, 2000. doi:10.1378/chest.118.3.795.

[17]Lieber, B. B., and Y. Zhao. Oscillatory flow in a symmetric bifurcation airway model. *Ann. Biomed. Eng.* 26:821–830, 1998. doi:10.1114/1.128.

[18]Marchak, B. E., W. K. Thompson, P. Duffty, T. Miyaki, M. H. Bryan, A. C. Bryan, and A. B. Froese. Treatment of RDS by high-frequency oscillatory ventilation: a preliminary report. *J. Pediatr.* 99:287–292, 1981. doi:10.1016/S0022-3476(81)80480-5.

[19]Mehta, S., J. Granton, R. J. MacDonald, D. Bowman, A. Matte-Martyn, T. Bachman, T. Smith, and T. E. Stewart. High-frequency oscillatory ventilation in adults: the Toronto experience. *Chest* 126:518–527, 2004. doi:10.1378/chest.126.2.518.

[20]Moganasundram, S., A. Durward, S. M. Tibby, and I. A. Murdoch. High-frequency oscillation in adolescents. *Br. J. Anaesth.* 88:708–711, 2002. doi:10.1093/bja/88.5.708.

[21]Nishida, M., Y. Inaba, and K. Tanishita. Gas dispersion in a model pulmonary bifurcation during oscillatory flow. *J. Biomech. Eng.* 119:309–316, 1997. doi:10.1115/1.2796095.

[22]Nowak, N., P. P. Kakade, and A. V. Annapragada. Computational fluid dynamics simulation of airflow and aerosol deposition in human lungs. *Ann. Biomed. Eng.* 31:374–390, 2003. doi:10.1114/1.1560632.

[23]Olson, D. E. Fluid mechanics relevant to respiration—flow within curved or elliptical tubes and bifurcating systems. Ph.D. Thesis, London University, London, 1971.

[24]Peattie, R. A., and W. Schwarz. Experimental investigation of oscillatory flow through a symmetrically bifurcating tube. *J. Biomech. Eng.* 120:584–593, 1998. doi:10.1115/1.2834748.

[25]Raffel, M., C. Willert, and J. Kompenhans. Particle Image Velocimetry: A Practical Guide. Berlin: Springer-Verlag, 1998.

[26]Ramuzat, A., and M. L. Riethmuller. PIV investigation of oscillating flows within a 3D lung multiple bifurcations model. 11th International Symposium on Application of Laser Techniques to Fluid Mechanics, Lisbon, Portugal, 2002.

[27]Rimensberger, P. C., M. Beghetti, S. Hanquinet, and M. Berner. First intention high-frequency oscillation with early lung volume optimization improves pulmonary outcome in very low birth weight infants with respiratory distress syndrome. *Pediatrics* 105:1202–1208, 2000. doi:10.1542/peds.105.6.1202.

[28]Rubenfeld, G. D. Epidemiology of acute lung injury. *Crit. Care Med.* 31:S276–284, 2003. doi:10.1097/01.CCM.0000057904.62683.2B.

[29]Schroter, R. C., and M. F. Sudlow. Flow patterns in models of the human bronchial airways. *Respir. Physiol.* 7:341–355, 1969. doi:10.1016/0034-5687(69)90018-8.

[30]Tanaka, G., T. Ogata, K. Oka, and K. Tanishita. Spatial and temporal variation of secondary flow during oscillatory flow in model human central airways. *J. Biomech. Eng.* 121:565–573, 1999. doi:10.1115/1.2800855.

[31]Tanaka, G., Y. Ueda, and K. Tanishita. Augmentation of axial dispersion by intermittent oscillatory flow. *J. Biomech. Eng.* 120:405–415, 1998. doi:10.1115/1.2798008.

[32]Taylor, G. Dispersion of soluble matter in solvent flowing slowly through a tube. *Proc. R. Soc. Lond. A Math. Phys. Sci.* 219:186–203, 1953. doi:10.1098/rspa.1953.0139.

[33]Taylor, G. The dispersion of matter in turbulent flow through a pipe. *Proc. R. Soc. Lond. A Math. Phys. Sci.* 223:446–468, 1954. doi:10.1098/rspa.1954.0130.
[34]Weibel, E. R. Morphometry of the Human Lung. New York: Academic Press, 1963.
[35]Womersley, J. R. Method for the calculation of velocity, rate of flow and viscous drag in arteries when their pressure gradient is known. *J. Appl. Physiol.* 127:553–563, 1955.